SUPPORTING INFORMATION for:

Under Pressure: Mechanochemical Effects on Structure and Ion Conduction in the Sodium-Ion Solid Electrolyte Na_3PS_4

Theodosios Famprikis [a,b,†,‡], Ulas Kudu [a], James A. Dawson [b,c], Pieremanuele Canepa [d], François Fauth [e], Emmanuelle Suard [f], Mohamed Zbiri [f], Damien Dambournet [g,‡], Olaf J. Borkiewicz [h], Houssny Bouyanfif [i], Steffen P. Emge [j], Sorina Cretu [a], Jean-Noël Chotard [a,l], Clare P. Grey [j,†], Wolfgang G. Zeier [l], M. Saiful Islam [b,†]* and Christian Masquelier [a,†,‡]**

[a]Laboratoire de Réactivité et Chimie des Solides (LRCS), CNRS UMR 7314, Université de Picardie Jules Verne, 80039 Amiens, France

[b]Department of Chemistry, University of Bath, BA2 7AY, United Kingdom

[c]Chemistry—School of Natural and Environmental Sciences, Newcastle University, Newcastle upon Tyne NE1 7RU, United Kingdom

[d]Department of Materials Science and Engineering, The National University of Singapore, 117576, Singapore

[e]CELLS – ALBA Synchrotron, Cerdanyola del Vallès, 08290 Barcelona, Spain ILL

[f]Institut Laue-Langevin (ILL), BP 156, 71 Avenue des Martyrs, 38042 Grenoble, France

[g]Physico-Chimie des Electrolytes et Nano-systèmes Interfaciaux (PHENIX), CNRS UMR 8234, Sorbonne Université, F-75005 Paris, France

[h]X-ray Science Division, Advanced Photon Source, Argonne National Laboratory, Argonne, Illinois, USA

[i]Laboratoire de Physique de la Matière Condensée (LPMC), UR 2081, Université de Picardie Jules Verne, Amiens 80039, France

[j]Department of Chemistry, University of Cambridge, CB2 1EW, United Kingdom

[k]Institute of Inorganic and Analytical Chemistry, University of Muenster, Correnstrasse 30, 48149 Muenster, Germany

[†]ALISTORE European Research Institute, CNRS FR 3104, 80039 Amiens, France

[‡]Réseau sur le Stockage Électrochimique de l'Énergie (RS2E), CNRS FR 3459, 80039 Amiens, France

Corresponding Authors

theo.famprikis@u-picardie.fr; m.s.islam@bath.ac.uk; christian.masquelier@u-picardie.fr

Rietveld refinements of Bragg diffractograms

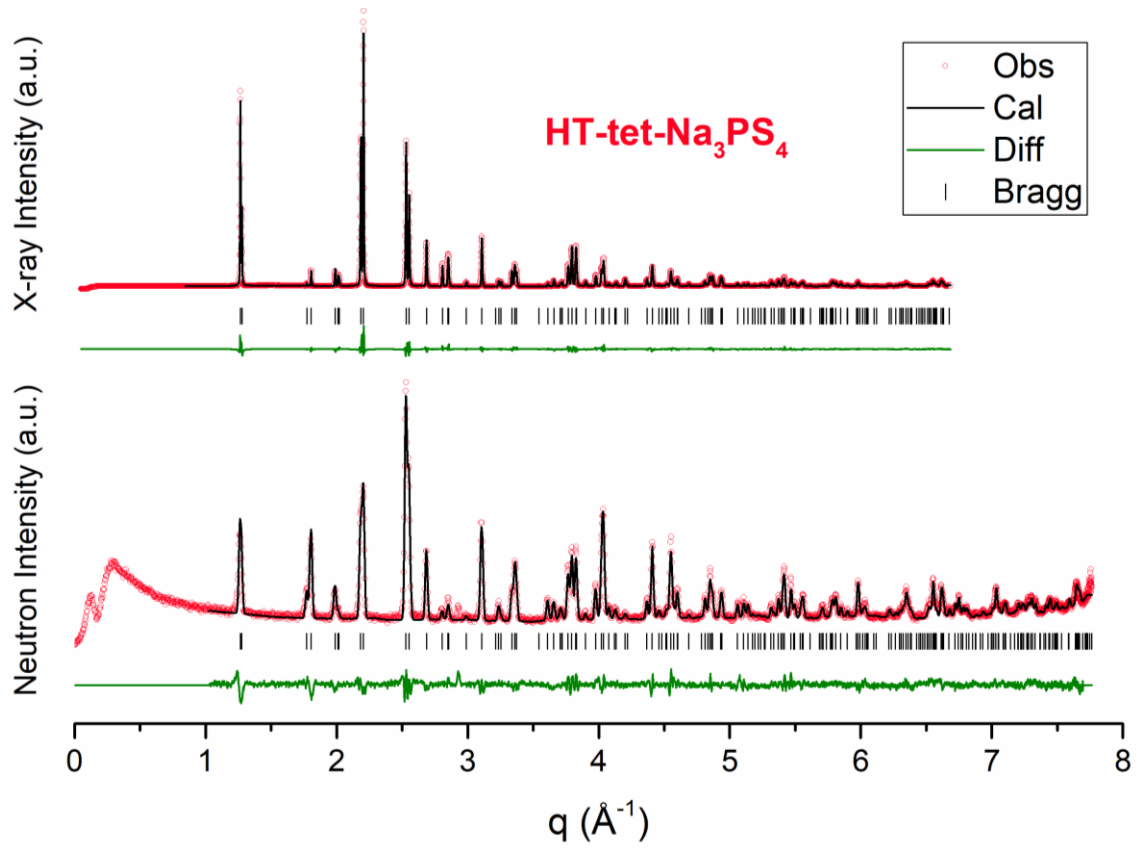

***Figure S1**: Rietveld refinements of the synchrotron x-ray and neutron diffractograms of the HT-tet-Na_3PS_4 sample. X-ray reliability parameters: R_p = 11.1, R_{wp} = 13.1, R_{exp} = 0.66, χ^2 = 397, R_{Bragg} = 4.73. Neutron reliability parameters: R_p = 24.5, R_{wp} = 19.5, R_{exp} = 11.31, χ^2 = 2.99, R_{Bragg} = 11.66.*

***Table S1**: Resulting structural parameters from combined Rietveld refinements of the synchrotron x-ray and neutron diffractograms of the HT-tet-Na_3PS_4 sample. Fitted parameters in bold. Space group $P\bar{4}2_1c$ (114),* ***a=6.9617(2) Å, c=7.0919(3) Å** (V/Z=171.86 Å³/f.u.)*

Atom	x	y	z	Wyckoff	Occupancy	B_{iso}
P	0	0	0	4d	1	**1.26(4)**
S	**0.1862(1)**	**0.1535(1)**	**0.1655(2)**	8e	1	**1.73(2)**
Na1	0	0.5	**0.0728(3)**	4d	1	**3.79(6)**
Na2	0	0	0.5	2b	1	**4.47(9)**

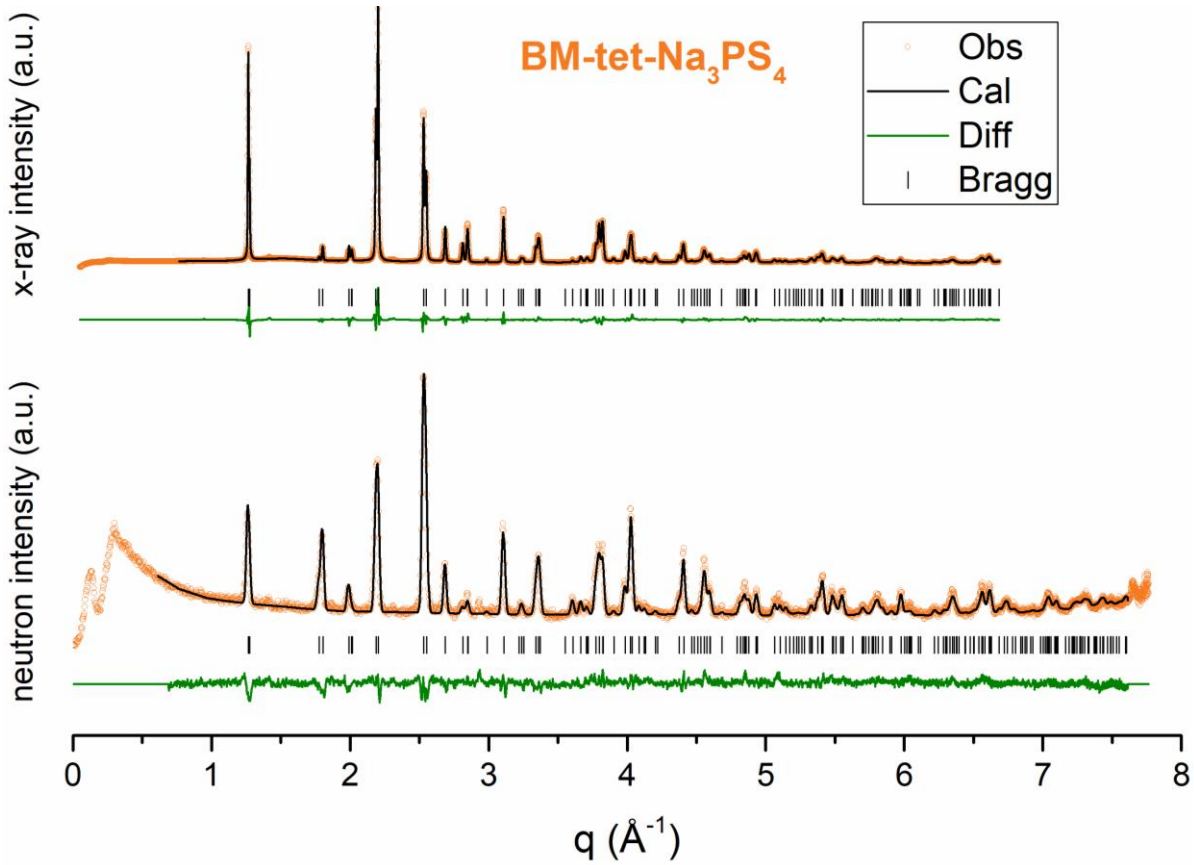

***Figure S2**: Rietveld refinements of the synchrotron x-ray and neutron diffractograms of the BM-tet-Na_3PS_4 sample. X-ray reliability parameters: R_p = 13.0, R_{wp} = 13.1, R_{exp} = 0.845, χ^2 = 239, R_{Bragg} = 6.19. Neutron reliability parameters: R_p = 29.9, R_{wp} = 21.9, R_{exp} = 13.9, χ^2 = 2.48, R_{Bragg} = 15.7.*

***Table S2**: Resulting structural parameters from Rietveld refinements of the synchrotron x-ray and neutron diffractograms of the BM-tet-Na_3PS_4 sample. Fitted parameters in bold. Space group $P\bar{4}2_1c$ (114),* ***a=6.9696(3) Å, c=7.0715(3) Å** (V/Z=171.71 Å³/f.u.)*

Atom	x	y	z	Wyckoff	Occupancy	B_{iso}
P	0	0	0	4d	1	**1.52(4)**
S	**0.1841(2)**	**0.1553(2)**	**0.1654(2)**	8e	1	**2.11(3)**
Na1	0	0.5	**0.0606(4)**	4d	1	**4.86(8)**
Na2	0	0	0.5	2b	1	**5.5(1)**

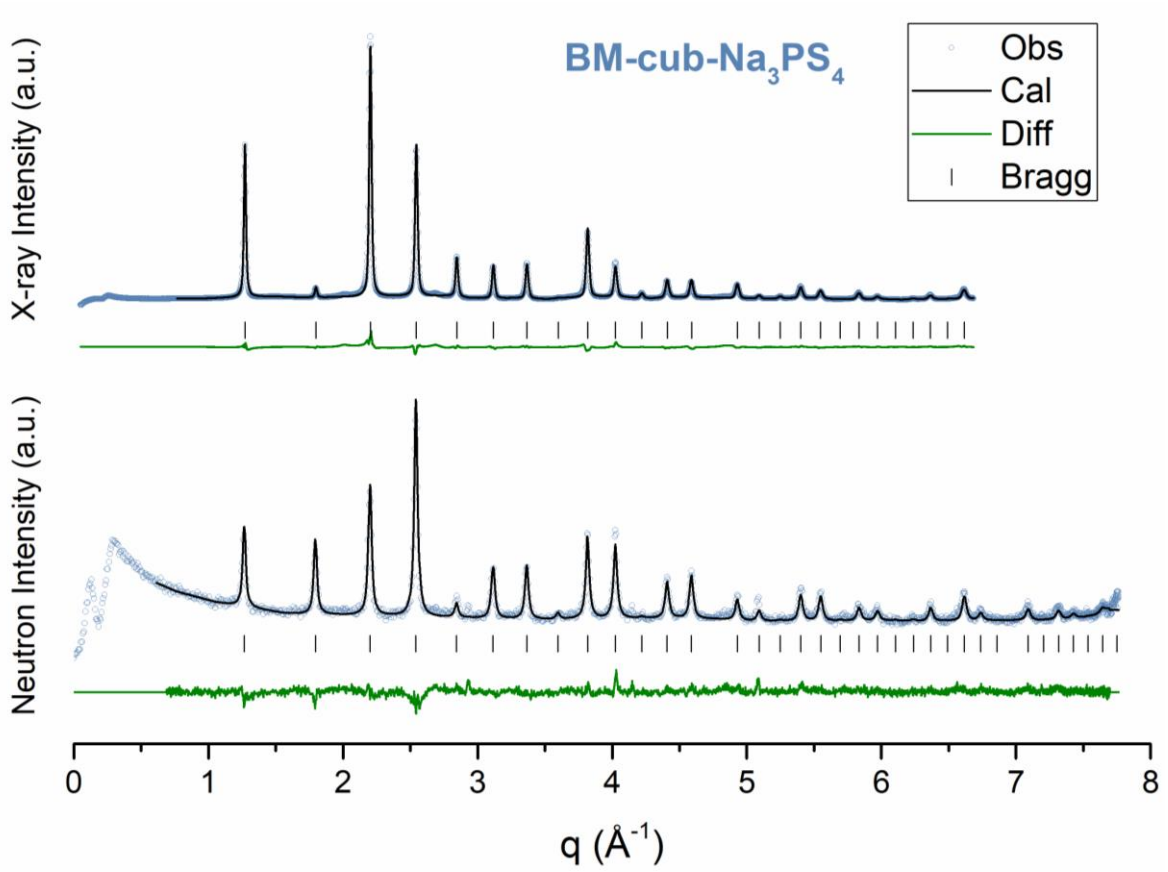

***Figure S3**: Rietveld refinements of the synchrotron x-ray and neutron diffractograms of the BM-cub-Na_3PS_4 sample. X-ray reliability parameters: R_p = 12.5, R_{wp} = 11.8, R_{exp} = 0.864, χ^2 = 186, R_{Bragg} = 6.82. Neutron reliability parameters: R_p = 33.0, R_{wp} = 23.5, R_{exp} = 16.7, χ^2 = 1.98, R_{Bragg} = 14.0.*

***Table S3**: Resulting structural parameters from Rietveld refinements of the synchrotron x-ray and neutron diffractograms of the BM-cub-Na_3PS_4 sample. Fitted parameters in bold. Space group $I\bar{4}3m$ (217), **a=6.978(2)** Å (V/Z=169.91 Å³/f.u.).*

Atom	x	y	z	Wyckoff	Occupancy	B_{iso}
P	0	0	0	2a	1	**2.14(4)**
S	**0.16799(8)**	(=x)	(=x)	8c	1	**3.24(3)**
Na	**0.0606(9)**	0.5	0	24f	0.25	**5.2(2)**

Discussion of Rietveld fit quality

It is noted that the discrepancy values related to the Rietveld refinement of the synchrotron x-ray diffractograms are quite high. This is in contrast with visual inspection of the fits that reveals a good agreement between observed and calculated intensities. This is related to the high precision of the data measured at the MSPD beamline of the ALBA synchrotron. Conventional factors used to judge the "wellness of fit" are computed the ratio observed difference (Y_{obs}-Y_{calc}) and standard uncertainty (inverse of precision). Consequently, higher data precision leads to higher χ^2, R_{wp} etc. Specifically in our case, minor imperfections (mainly in the peak shapes and the background) that cannot be modelled, generate these large discrepancy values. This interpretation is supported by the fact that profile (i.e. LeBail) fits of the same data result in similar values for the wellness of fit indices, showing that there is no significant error in our crystallographic model. Such effects are well-known in the literature[1].

Group-subgroup relationship between α- and β-Na_3PS_4

***Table S4**: Group-subgroup relationship of the different atomic positions in the polymorphs of Na_3PS_4. 25%-occupied Na3 offers an alternative description to Na1+Na2.*

Atom	$P\bar{4}2_1c$ (114)		$I\bar{4}2m$ (121)		$I\bar{4}3m$ (217)	
	Wyckoff	**Point Grp.**	**Wyckoff**	**Point Grp.**	**Wyckoff**	**Point Grp.**
P	2a (0, 0, 0)	$\bar{4}$	2a (0, 0, 0)	$\bar{4}2m$	2a (0, 0, 0)	$\bar{4}3m$
S	8e (x, y, z)	1	8i (x, x, z)	$..m$	8c (x, x, x)	$.3m$
Na1	4d (0, ½, z)	2	4c (0, ½, 0)	222	6b (0, ½, ½)	$\bar{4}2m$
Na2	2b (0, 0, ½)	$\bar{4}$	2b (0, 0, ½)	$\bar{4}2m$		
(Na3)			$8g_1$ (x_1, 0, ½) $8g_2$ (x_2, 0, ½) 8h (0, ½, z)	.2. .2. 2..	24f (x, ½, 0)	2..

Williamson-Hall plot

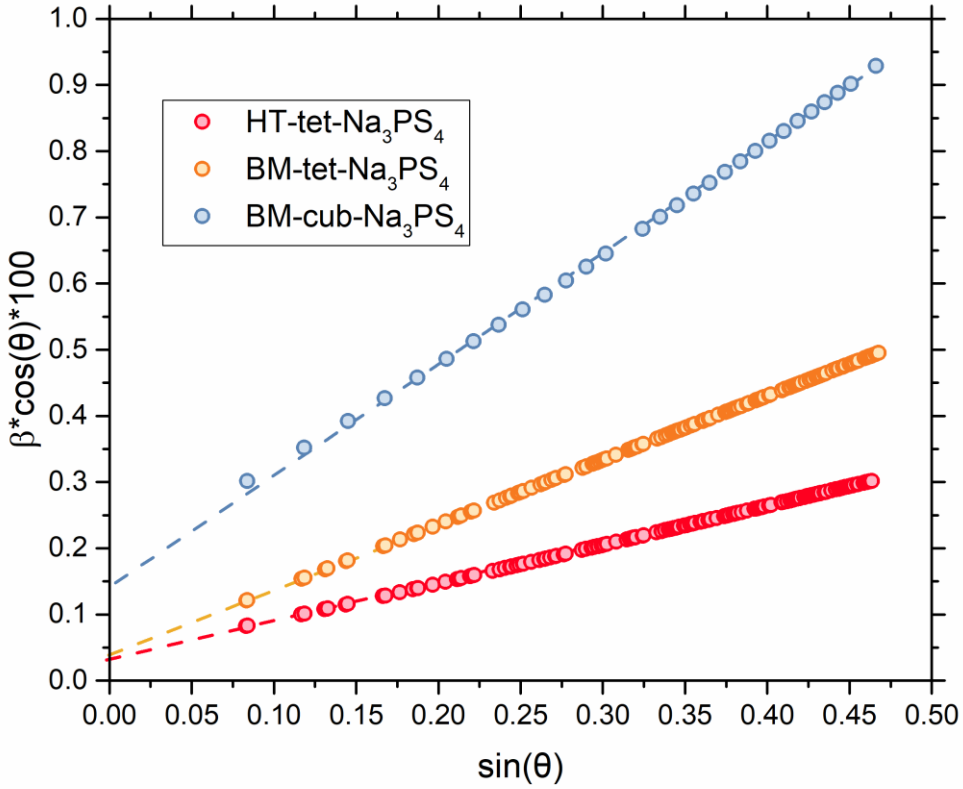

***Figure S4**: Williamson-Hall plot of the diffraction peak broadening of Na_3PS_4 samples from synchtrotron x-rays. The peak width (β) here includes instrumental broadening, which was nevertheless subtracted for the quantitative analysis presented in the main text. The inverse of the y-intercept corresponds to the crystallite size which is similar for HT-tet and BM-tet but much smaller for BM-cub. The slope corresponds to the microstrain, increasing from HT-tet to BM-tet to BM-cub.*

Comparison of the x-ray PDFs

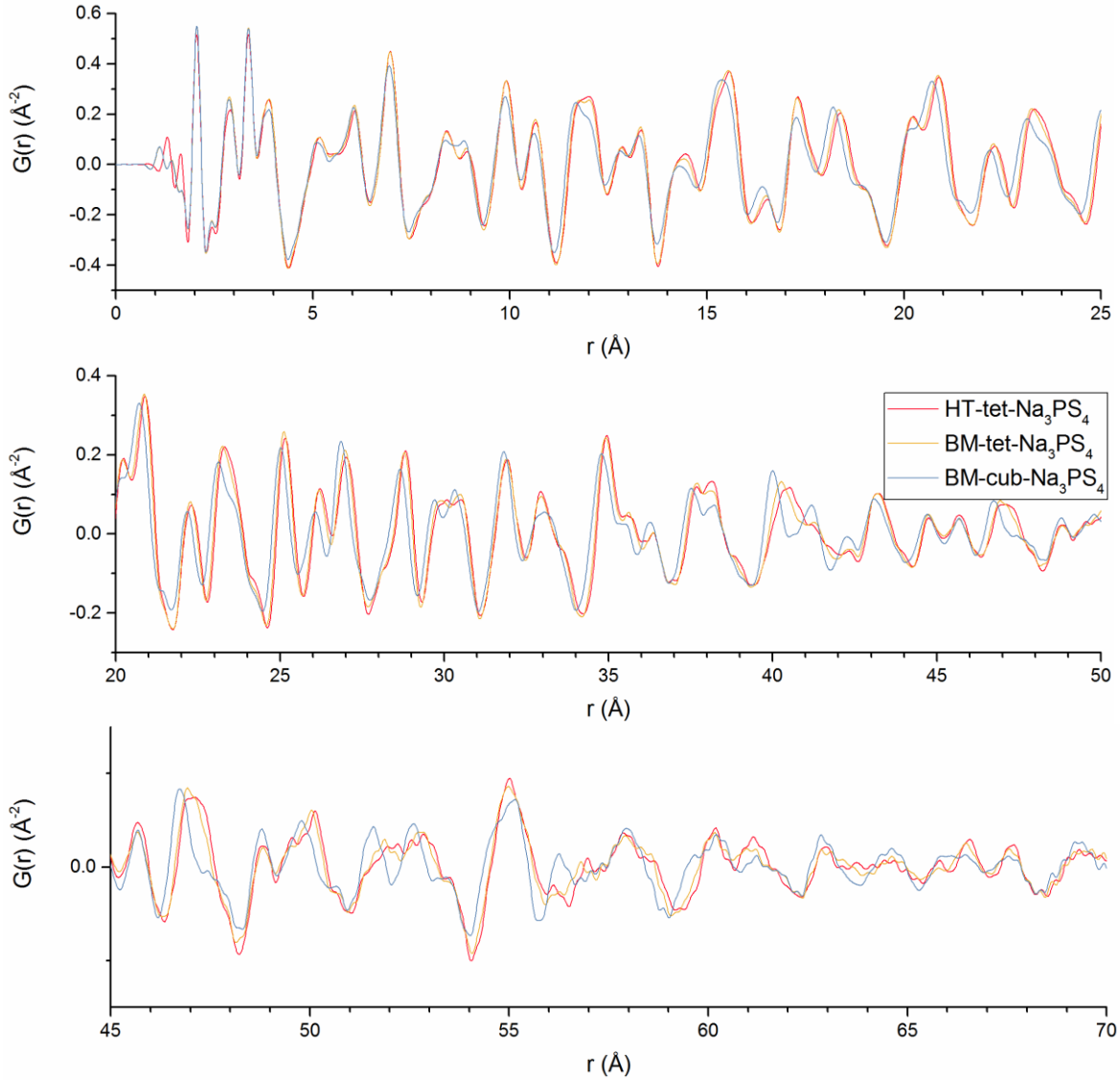

***Figure S5**: Comparison of the synchrotron x-ray PDF of the Na_3PS_4 samples divided into (a) short- (b) – medium- and (c) long-range correlations.*

Refinements of the full x-ray PDFs

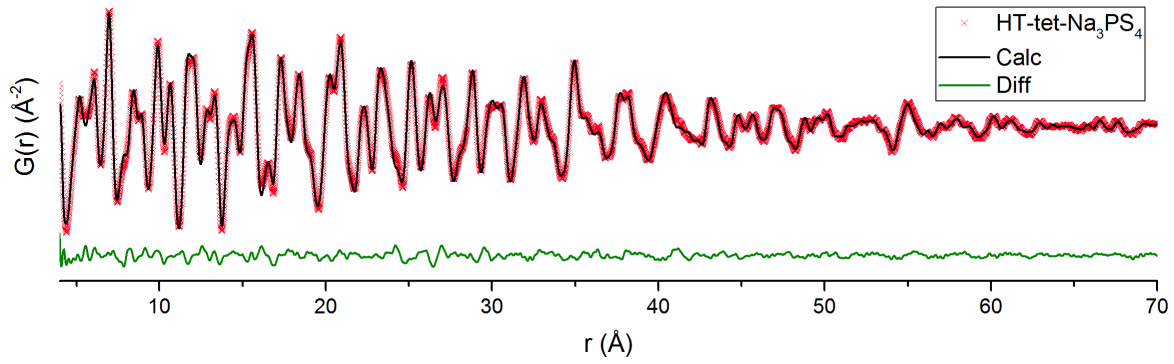

***Figure S6**: Structural refinement of the synchrotron x-ray PDF of the HT-tet-Na_3PS_4 sample. R_w=0.103*

***Table S5**: Resulting structural parameters from structural refinements of the x-ray PDF of the HT-tet-Na_3PS_4 sample in the range 4-70 Å. Fitted parameters in bold. Space group $P\bar{4}2_1c$ (114), a=**6.97** Å, c=**7.11** Å (V/z=172.7 Å³/f.u.). *Na ADPs shown in Table S6*

Atom	x	y	z	Wyckoff	Occupancy	B_{iso}
P	0	0	0	4d	1	**0.88**
S	**0.186**	**0.152**	**0.165**	8e	1	**1.83**
Na1	0	0.5	**0.072**	4d	1	**4.63***
Na2	0	0	0.5	2b	1	**5.66***

***Table S6**: Anisotropic thermal displacement parameters for Na in HT-tet-Na_3PS_4*

v	β_{11}	β_{22}	β_{33}	β_{12}	β_{13}	β_{23}
Na1	**0.027**	**0.011**	**0.027**	**0**	0	0
Na2	**0.040**	$=\beta_{11}$	**0.007**	0	0	0

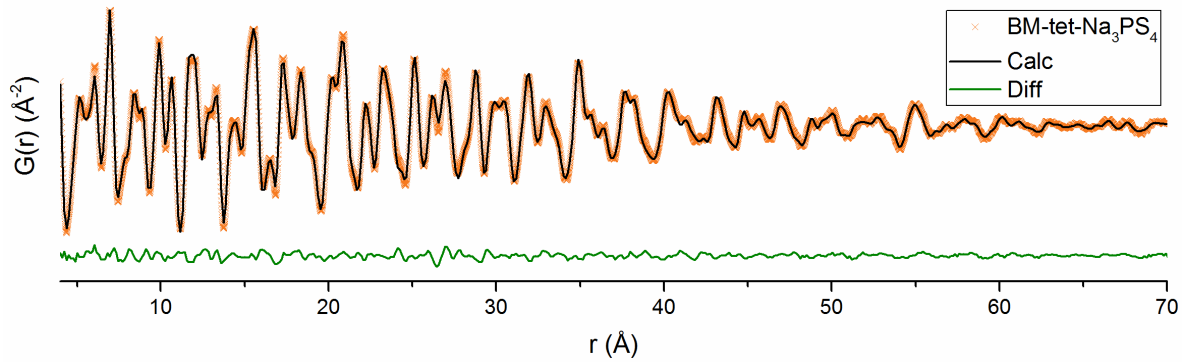

***Figure S7**: Structural refinement of the synchrotron x-ray PDF of the BM-tet-Na_3PS_4 sample. R_w=0.090*

***Table S7**: Resulting structural parameters from structural refinements of the x-ray PDF of the BM-tet-Na_3PS_4 sample in the range 4-70 Å. Fitted parameters in bold. Space group $P\bar{4}2_1c$ (114), a=**6.97** Å, c=**7.09** Å (V/z=172.3 Å³/f.u.). *Na ADPs shown in Table S8*

Atom	x	y	z	Wyckoff	Occupancy	B_{iso}
P	0	0	0	4d	1	**1.07**
S	**0.186**	**0.154**	**0.164**	8e	1	**2.12**
Na1	0	0.5	**0.070**	4d	1	**4.73***
Na2	0	0	0.5	2b	1	**6.36***

***Table S8**: Anisotropic thermal displacement parameters for Na in BM-tet-Na_3PS_4*

Atom	β_{11}	β_{22}	β_{33}	β_{12}	β_{13}	β_{23}
Na1	**0.033**	**0.016**	**0.024**	0	0	0
Na2	**0.045**	$=\beta_{11}$	**0.007**	0	0	0

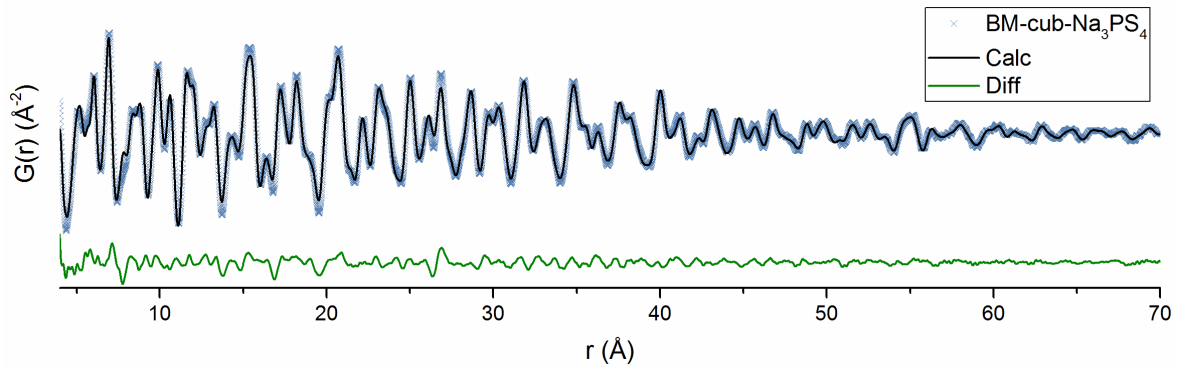

***Figure S8**: Structural refinement of the synchrotron x-ray PDF of the BM-cub-Na_3PS_4 sample constrained in the **$P\bar{4}2_1c$** symmetry. R_w=0.154*

***Table S9**: Resulting structural parameters from structural refinements of the x-ray PDF of the BM-cub-Na_3PS_4 sample in the range 4-70 Å. Fitted parameters in bold. Space group $P\bar{4}2_1c$ (114), a=**7.00** Å, c=**6.97** Å (V/z=170.7 Å³/f.u.). *Na ADPs shown in Table S10*

Atom	x	y	z	Wyckoff	Occupancy	B_{iso}
P	0	0	0	4d	1	**1.98**
S	**0.184**	**0.160**	**0.161**	8e	1	**4.11**
Na1	0	0.5	**0.062**	4d	1	**7.77***
Na2	0	0	0.5	2b	1	**12.33***

***Table S10**: Anisotropic thermal displacement parameters for Na in BM-cub-Na_3PS_4*

Atom	β_{11}	β_{22}	β_{33}	β_{12}	β_{13}	β_{23}
Na1	**0.058**	**0.019**	**0.042**	0	0	0
Na2	**0.080**	=β_{11}	**0.029**	0	0	0

Fitting of calculated Pressure-Volume-Energy data

Our static DFT calculations of the energy and volume of α- and β-Na_3PS_4 as a function of pressure allow the determination of the bulk modulus of the two polymorphs through fitting our results to the Birch-Murnaghan equation of state:

$$P(V) = \frac{3B_0}{2}\left[\left(\frac{V_0}{V}\right)^{\frac{7}{3}} - \left(\frac{V_0}{V}\right)^{\frac{5}{3}}\right]\left\{1 + \frac{3}{4}\left(\frac{dB}{dP} - 4\right)\left[\left(\frac{V_0}{V}\right)^{\frac{2}{3}} - 1\right]\right\} \quad (S1)$$

where V_0 is the equilibrium (unit cell) volume (at P=0), B_0 is the isothermal bulk modulus (at P=0) and dB/dP is the derivative of the bulk modulus with respect to pressure. The results are shown in Table S11 and Figure S9.

***Table S11**: Results of fitting the DFT-calculated energies versus volume using the Birch-Murnaghan equation of state.*

Polymorph	V_0 (Å^3)	B_0 (GPa)	dB/dP (-)
α-Na_3PS_4 ($P\bar{4}2_1c$)	329.17	26.8	4.7
β-Na_3PS_4 ($I\bar{4}3m$)	327.59	27.9	4.8

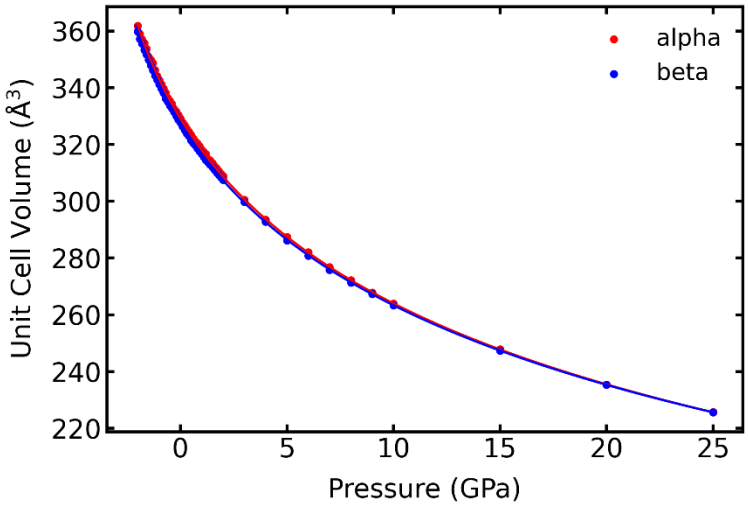

***Figure S9**: Variation of the volume between α- and β-Na_3PS_4 and associated fits to the Birch-Murnaghan equation of state as a function of pressure.*

Summary of fits of the diffractograms of BM-cub-Na_3PS_4

For the Rietveld refinements of the Bragg diffractograms the wellness-of-fit index χ^2 was utilized to quantify the appropriateness of different descriptions for the Na distribution. Since these correspond to combined refinements of the synchrotron x-ray- and neutron datasets and a combined χ^2 was utilized, defined as:

$$\chi^2 = 0.01\chi^2_{x-ray} + 0.99\chi^2_{neutron} \ (S2)$$

For the PDF refinements of the total scattering diffractograms the wellness-of-fit index R_w was utilized. In both cases a lower value indicates a better fit.

***Table S12**: Results of the Rietveld and PDF refinements of BM-cub-Na_3PS_4. Site labels refer to the Wyckoff sites the respective space group, B and β_{ii} refer to isotropic and anisotropic displacement parameters (ADPs) respectively, x is fractional coordinate of Na in the lattice and occ. stands for occupancy. Rietveld- and PDF refinements carried out in the ranges 0.8-6.7 $Å^{-1}$ and 4-20 Å, respectively.*

Space Group	Na description	Number of Na refined parameters	Rietveld refinement result (χ^2)	x-ray PDF refinement result (R_w)
$I\bar{4}3m$	1x 6b site	1 (B_{iso})	4.600	0.188
	1x 12d site	1 (B_{iso})	38.06	0.445
	1x 24f site	2 (x_{24f}, B_{iso})	4.182	0.171
	1x 24g site	3 (x_{24g}, z_{24g}, B_{iso})	4.274	0.173
	2x 6b and 12d sites	3 (2xB_{iso}, occ.)	4.436	0.188
	2x 24f and 12d sites	4 (x_{24f}, 2xB_{iso}, occ.)	3.999	0.171
	2x 24g and 12d sites	5 (x_{24g}, z_{24g}, 2xB_{iso}, occ.)	4.065	0.173
	1x 6b site with ADPs	2 (β_{11}, β_{22})	4.113	0.182
	1x 24f site with ADPs	5 (x_{24f}, β_{11}, β_{22}, β_{33}, β_{23})	4.052	**0.167**
	1x 24g site with ADPs	6 (x_{24g}, z_{24g}, β_{11}, β_{22}, β_{12}, β_{13})	4.192	0.171
$I\bar{4}2m$	2x 4c and 2b	2 (2xB_{iso})		0.179
	2x 4c and 2b with ADPs	5(2xβ_{11}, 1xβ_{22}, 2xβ_{33})		0.171
	3x $8g_1$, $8g_2$ and 8h	6(x_{8g1}, x_{8g2}, z_{8h}, 3xB_{iso})		0.160
	3x $8g_1$, $8g_2$ and 8h with ADPs	12 (x_{8g1}, x_{8g2}, z_{8h}, 3xβ_{11}, 3xβ_{22}, 3xβ_{33})		0.149
$P\bar{4}2_1c$	2x 4d and 2d	3 (z_{4d}, 2xB_{iso})		0.117
	2x 4d and 2d with ADPs	7 (z_{4d}, 2xβ_{11}, β_{22}, 2xβ_{33}, β_{12})		**0.107**

Additional solid-state NMR experimental details

Further NMR experiments not described in the main text were performed at 9.4 T (Avance I console) and 16.4 T (Avance III console) using a Bruker double-resonance 7.0 mm MAS probe at 4 kHz MAS with optional laser heating of the sample. Spectra were measured using regular zg/one-pulse pulse programs with π/6 or π/2 pulse lengths for ^{23}Na on the 9.4 T or 16.4 T magnets respectively. Powder samples of HT-tet Na_3PS_4 were packed between layers of dried KBr under argon atmosphere inside a glovebox (M. Braun; $p(O_2)/p^o < 1$ ppm, $p(H_2O)/p^o < 1$ ppm) in BN or AlN inserts inside 7.0 mm ZrO_2 rotors (Bruker) shortly before the measurement. The spectra were externally referenced against 0.1 M NaCl aqueous solution (0 ppm) for ^{23}Na. The reference compounds were used for pulse length optimization. The ^{23}Na spectra were fitted with DMFIT software to obtain values of C_Q and η_Q using the *Q-MAS 1/2* model to fit the central transition.T hese fits using the same quadrupolar parameters show good agreement (Table S17). The worst fit is obtained at the lowest field due to a combination of low field strength (9.4 T) and slow MAS rate (4 kHz). This partially invalidates the model assumption used for the fit, i.e. infinitely fast MAS removing other interactions.

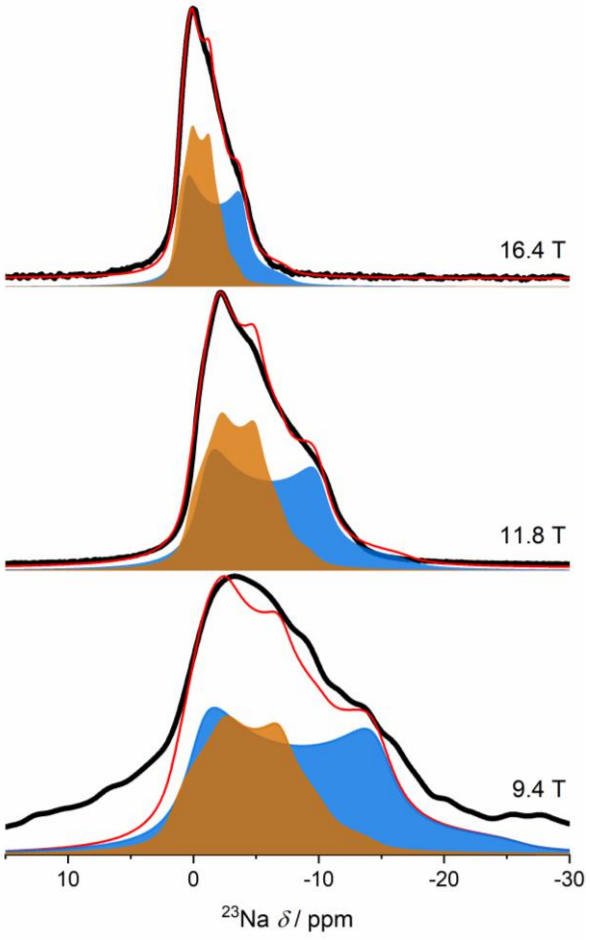

***Figure S10**: ^{23}Na-NMR of α-Na_3PS_4 at different fields (9.4 T & 16.4 T = 4 kHz MAS; 11.8 T = 25 kHz MAS). Spectra were fitted using the same parameters and only amplitude and chemical shift positions were optimized.*

***Table S13**: Summary of parameters obtained from the fits at different fields, Signal 1 (C_Q=2.3 kHz, η =0) Signal 2 (C_Q =1.7 kHz, η=0.44)*

Field / T	δ_{iso} (Signal 1) / ppm	δ_{iso} (Signal 2) / ppm	Signal 1 : Signal 2 / %	$\Delta\delta_{iso}$(1-2)/ppm
16.4	3.76	2.28	63:37	1.48
11.8	1.76	0.89	55:45	0.87
9.4	2.11	1.69	52:48	0.42

Derivation of the activation volume formula

From the typical definitions for diffusion (S3), conductivity (S4) and the Nernst-Einstein relationship (S5):

$$D = z{a_0}^2 \nu_0 e^{-\frac{\Delta G}{k_B T}} \ (S3)$$

$$\sigma = qnu \ (S4)$$

$$D = \frac{uk_B T}{q} \ (S5)$$

where, D: diffusivity, σ: ionic conductivity, z: a geometrical constant of order unity, α_o: a characteristic (often "jump-") distance, ν_o: a characteristic (often "attempt-" or "Debye-") frequency, ΔG: the Gibbs free (often "activation-") energy for diffusion, k_B: the Boltzmann constant, T: temperature, q: the charge of diffusing ion, n: the concentration of mobile species, u: the mobility of mobile species; we obtain the following typical "Arrhenius" expression for ionic conductivity (S6):

$$\sigma T = \sigma_0 e^{-\frac{\Delta G}{k_B T}}, with\ \sigma_0 = \frac{znq^2 {a_0}^2 \nu_0}{k_B} \ (S6)$$

The activation volume, V_a, is then defined as the partial derivative of ΔG with pressure, P, at constant temperature:

$$V_a = (\frac{\partial \Delta G}{\partial P})_T = -k_B T(\frac{\partial \ln(\sigma)}{\partial P})_T + k_B T\left(\frac{\partial \ln(\sigma_0)}{\partial P}\right)_T \ (S7)$$

The first term in (S7) is directly observable in variable-pressure ionic conductivity measurements. For the Arrhenius prefactor, σ_o, in the second term in (S7), we assume that z, n and q are pressure invariant in the absence of a phase transition or change in diffusion mechanism. Thus, the second term in (S7) becomes:

$$k_B T(\frac{\partial \ln(\sigma_0)}{\partial P})_T = k_B T(\frac{\partial \ln({a_0}^2)}{\partial P})_T + k_B T(\frac{\partial \ln(\nu_0)}{\partial P})_T \ (S8)$$

The characteristic distance, α_o, is assumed to vary in analogy with the cubic lattice parameter α, so that $d\ln(\alpha_o^2)=d\ln(\alpha^2)$, and $\alpha^3=V$, the lattice volume. Then using the definitions for the compressibility, β, and the microscopic Grüneisen parameter, γ:

$$\beta = -\frac{1}{V}\frac{dV}{dP} \ (S9)$$

$$\gamma = -\frac{dln(\nu)}{dln(V)} \ (S10)$$

the first term in (S8) can be written:

$$k_B T(\frac{\partial \ln({a_0}^2)}{\partial P})_T = -k_B T\beta a^3(\frac{\partial \ln(a^2)}{\partial a^3})_T = -\frac{2k_B T\beta}{3} \ (S11)$$

And the second term in (S8):

$$k_B T(\frac{\partial \ln(\nu_0)}{\partial P})_T = k_B T\gamma\beta \ (S12)$$

So that from (S7)-(S12) the final equation for the activation volume:

$$V_a = k_B T(\beta\left(\gamma - \frac{2}{3}\right) - \frac{\partial \ln(\sigma)}{\partial P})_T \quad (S13)$$

When data for γ is unavailable, it is often assumed that γ=1 so that:

$$V_a = k_B T(\frac{\beta}{3} - \frac{\partial \ln(\sigma)}{\partial P})_T \ (S14)$$

as used in the main text.

Literature data on the compressibility of Na_3PS_4

***Table S14**: Reported values for the bulk modulus of Na_3PS_4*

Sample	Bulk Modulus (GPa)	Technique (ref.)
BM-Na_3PS_4 pressed @ 160 °C, 360 MPa	20.4	Ultrasonic Pulse-Echo exp. ([2])
BM-Na_3PS_4 pressed @ RT, 360 MPa	13.9	
BM-Na_3PS_4 pressed @ RT, 180 MPa	8.0	
tetragonal α-Na_3PS_4	25.3	DFT stress-strain calc. ([3])
cubic β-Na_3PS_4	21.5	
tetragonal α-Na_3PS_4	25.7-28.3	DFT Birch-Murnaghan ([4])
tetragonal α-Na_3PS_4	26.2	DFT stress-strain calc. ([5])
cubic β-Na_3PS_4	26.0	
tetragonal α-Na_3PS_4	26.8	DFT Birch-Murnaghan (this work)
cubic β-Na_3PS_4	27.9	

Determination of activation volume of Na_3PS_4

Assuming B = 25 GPa (β = 0.04 GPa^{-1}), the first and second terms of equation (S14) for the two Na_3PS_4 samples measured in this work are tabulated below.

$$V_a = k_B T\left(\frac{\beta}{3} - \frac{\partial \ln(\sigma)}{\partial P}\right)_T \quad (S14)$$

Table S15: Measured $\frac{\partial ln(\sigma)}{\partial P}$ slopes, compressibility corrections and derived activation volumes for the Na_3PS_4 samples measured in this work.

Sample	Measured $k_B T \frac{\partial \ln(\sigma)}{\partial P}$	Assumed $k_B T\beta/3$	Derived V_a
HT-tet-Na_3PS_4	-1.75 ± 0.02 cm^3/mol (= -2.91 ± 0.03 Å^3)	0.033 cm^3/mol (= 0.055 Å^3)	1.78 ± 0.02 cm^3/mol (= 2.97 ± 0.03 Å^3)
BM-cub-Na_3PS_4	-2.30 ± 0.04 cm^3/mol (= -3.81 ± 0.06 Å^3)	0.033 cm^3/mol (= 0.055 Å^3)	2.33 ± 0.04 cm^3/mol (= 3.87 ± 0.06 Å^3)

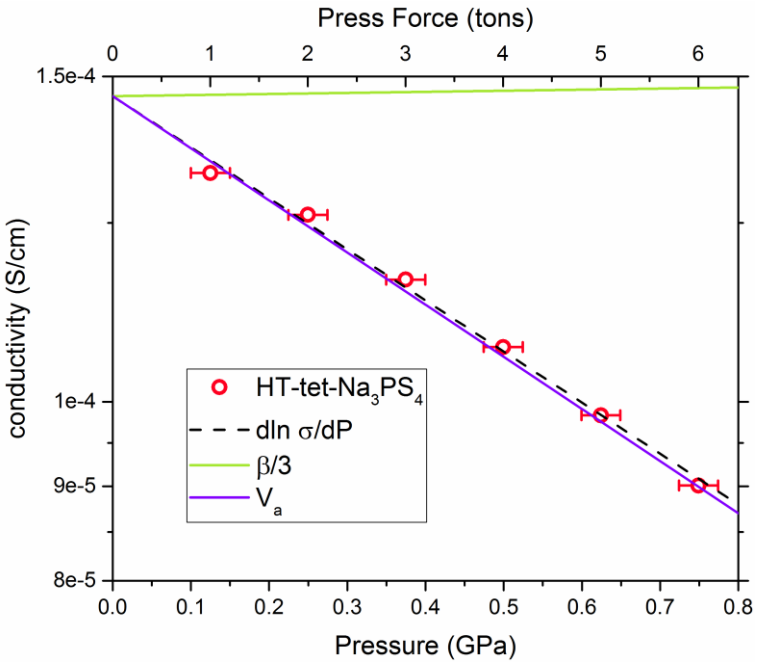

***Figure S11**: Deconvolution of the terms used in the calculation of the activation volume for HT-tet-Na_3PS_4*

Fitted capacitances of Na_3PS_4 from variable-pressure impedance spectra

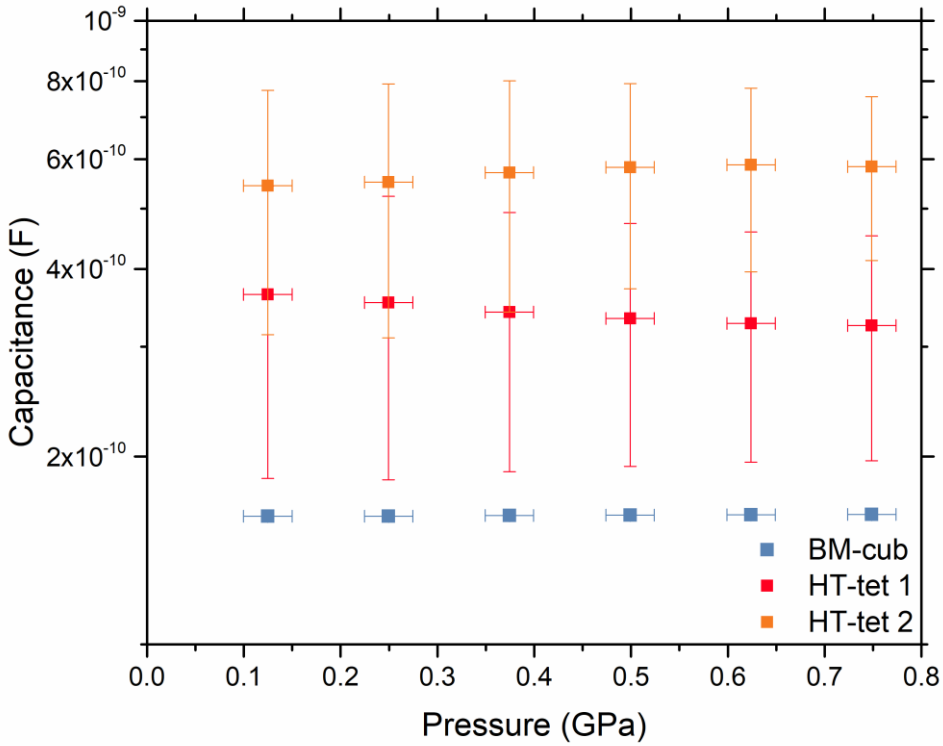

***Figure S12**: Evolution of the capacitance as a function of uniaxial pressure for HT-tet- and BM-cub-Na_3PS_4.*

Determination of activation volume of Na_3SbS_4

The volume and ionic conductivity dependence on pressure for Na_3SbS_4 was extracted from the published data sets of Wang et al. [6]

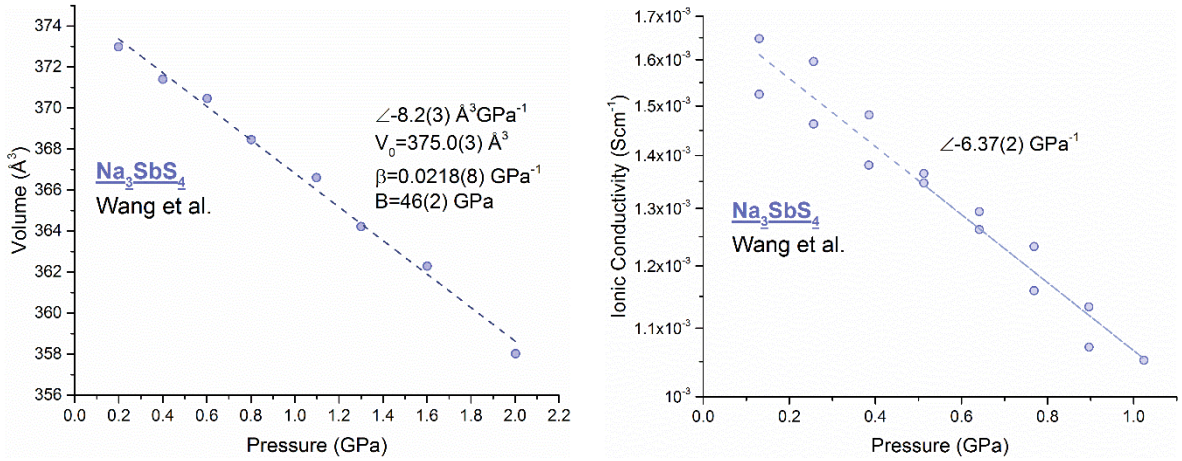

***Figure S13**: Extraction of the compressibility and activation volume of Na_3SbS_4 from the pressure evolution of crystallographic volume (a) and ionic conductivity (b). Data extracted from Wang et al.* [6]

The compressibility (bulk modulus) was calculated using eq. (S9)

$$\beta = -\frac{1}{V_0}\frac{dV}{dP} (= B^{-1}) \ (S9)$$

The resulting value of 46 GPa for the bulk modulus from diffraction data is rather surprising in comparison to the value of ~25 GPa for Na_3PS_4 (from different methodologies; see Table S14): one would intuitively expect Na_3SbS_4 to be softer.

The activation volume was then calculated using eq. (S14)

$$V_a = k_B T\left(\frac{\beta}{3} - \frac{\partial \ln(\sigma)}{\partial P}\right)_T \ (S14)$$

Table S16: Measured $\frac{\partial \ln(\sigma)}{\partial P}$ slope, compressibility correction and derived activation volume for Na_3SbS_4 measured by Wang et al. [6]

Sample	Measured $k_B T \frac{\partial \ln(\sigma)}{\partial P}$	Measured $k_B T\beta/3$	Derived V_a
Na_3SbS_4	-1.18 ± 0.08 cm³/mol (= -1.96 ± 0.13 Å³)	0.018 cm³/mol (= 0.030 Å³)	1.20 ± 0.08 cm³/mol (= 1.99 ± 0.13 Å³)

Chronological evolution of conductivity in HT-tet-Na_3PS_4 under pressure

Figure S14 represents the chronological evolution of the RT ionic conductivity of the HT-tet sample during the in-situ variable pressure experiments. A distinct ten-fold increase in conductivity is observed upon initial pressing up to ~0.25 GPa (Figure S14a). Following that, the conductivity decreases with applied pressure. Upon releasing the pressure and repeating the measurements in the direction of increasing pressure, the overall behavior is mostly reproducible, although the conductivity at 0 GPa does not return to the original value corresponding to HT-tet-Na_3PS_4 (panels b, c). Measurements in the reverse direction (of decreasing pressure) show increasing conductivity and demonstrate the reversibility of the effect of pressure (panels d, e). Panel f superimposes the conductivity data from the previous cycles of measurement and highlights two global domains of conductivity evolution. Varying the pressure between 0.25 and 1.5 GPa follows a constant $\frac{\partial \ln(\sigma)}{\partial P}$ slope from which the activation volume can be extracted. This corresponds to the reversible intrinsic response of the material to an applied pressure. The variability of conductivity close to 0 GPa (no applied pressure) corresponds to the irreversible extrinsic response of the pellet as a whole and is likely related to mesostructural effects (consolidation) as discussed in the main text.

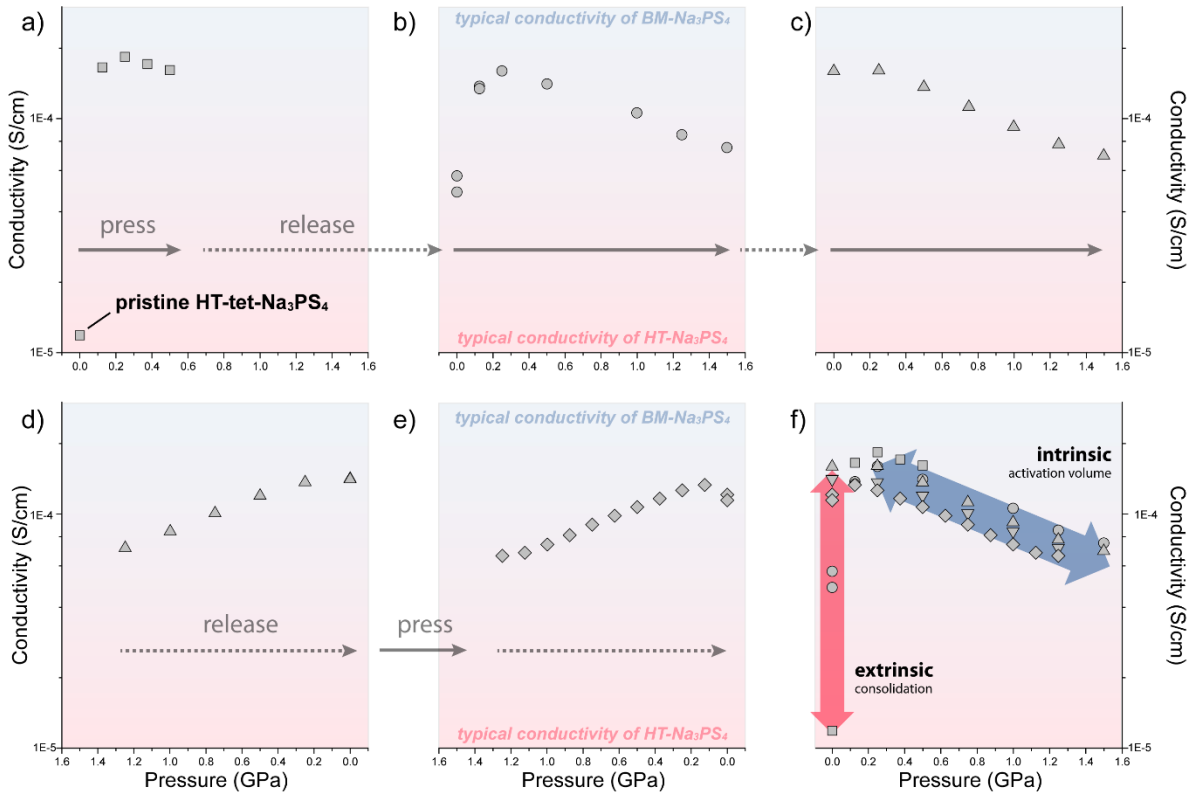

***Figure S14**: Chronological evolution of the in-situ pressure-impedance experiment on the HT-tet-Na_3PS_4 sample. Panels a) to c) show the evolution of measured conductivity while pressing (increasing pressure). Panels d) and e) show the evolution of measured conductivity on release (decreasing pressure, x-axis reversed). panel f) consists of an overlay of data points from panels a)-e). The axis scales are matched for all panels.*

Transmission electron microscopy

A transmission electron microscopy (TEM) analysis using a Tecnai F20 S-TWIN operating at 200 kV was performed in order to determine the morphology and the crystal structure of the Na_3PS_4 samples. The analyzed powders were sealed in glass flacons under Ar in order to prevent reaction with ambient moisture during transfer from the glovebox. For analysis, the samples were dispersed on standard carbon coated copper grids. Sample manipulation was performed under manual Ar flow until the holder was placed in the TEM column in order to minimize sample reaction with air. As thiophosphate materials are highly sensible to the electron beam dose the TEM measurements were limited to low magnification TEM imaging for morphological studies and selected area electron diffraction for structural/phase analysis. The required dose for these measurements can be kept below a few hundred $e^-/nm^2 \cdot s$, that is consider to be below the threshold at which structural and morphological changes appear in thiophosphate materials. High electron dose will lead to phase separation and material evaporation, mostly due the Na and P reaction with residual O_2 inside the microscope column and S sublimation.

Figure S15a shows the general morphology of HT-tet-Na_3PS_4 sample where it can be noticed that the sample is mostly composed of clusters of agglomerated particles with sizes varying between a few hundreds of nm to 1.5 um. Panel b shows a micrometer particle plate and the presence of small nanoparticles inside of it (panel d). Panel c displays the electron diffraction pattern of HT-tet-Na_3PS_4 indexable to α-Na_3PS_4.

Despite the high crystallinity of the sample evident from the diffraction analysis, multiple non-diffracting particles were found during the TEM analysis, suggesting a possible interaction between the sample and air during the holder transfer process to the TEM column or an interaction with the electron beam. These effects were qualitatively worse on ball-milled samples. In order to minimize the beam effects on the sample, cryo-TEM analysis was also performed, but the sample showed the same instability during electron beam exposure at the higher electron doses needed for high resolution images.

A possible experiment that might improve the quality of the acquired data is using a higher acceleration voltage TEM machine (300kV). This will decrease the effect of radiolysis beam damage that is the predominate damage mechanism for electrical insulators. Using low dose TEM by taking advantage of the new direct electron detection cameras is also possible. A transfer holder under vacuum or Ar atmosphere from the glovebox to the TEM column without exposure of the in air atmosphere can also be considered in order to separate the effect of the electron beam from the one of ambient exposure.

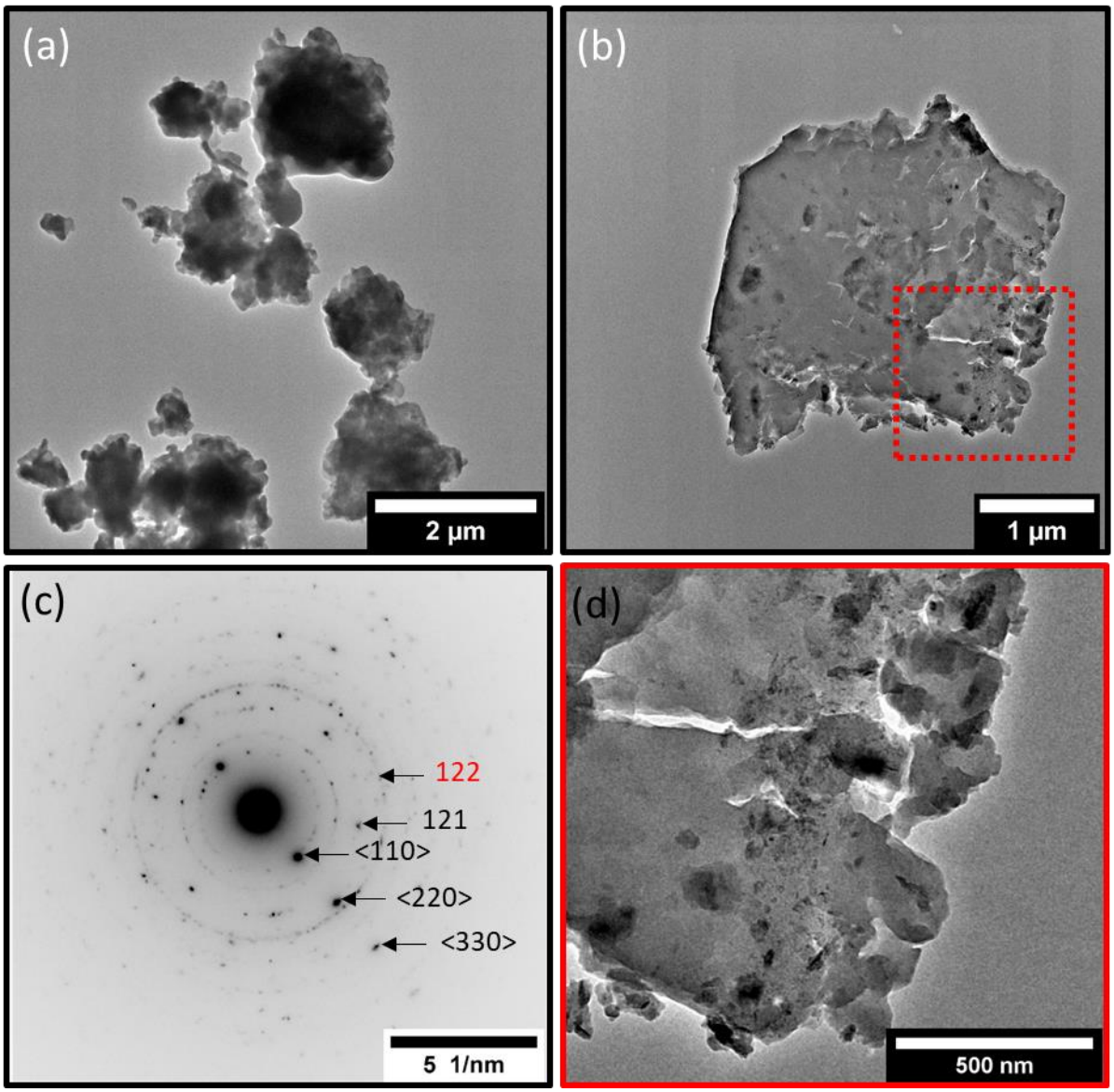

Figure S15. *(a)(b)(d) Transmission electron micrographs of HT-tet-Na_3PS_4; (c) electron diffraction patterns of tetragonal Na_3PS_4*

Assumptions and limitations of the variable-pressure impedance spectroscopy setup

It should be noted that the variable-pressure impedance measurements reported herein have been performed on a rather primitive setup, originally designed for SSB cycling [7] and not adapted to pressure experiments. Consequently, our analysis hinges on several assumptions, which we discuss below along with propositions for further refinement of instrumentation and protocols.

The first assumption we have adopted is that of complete densification of our samples under the applied pressure. **The ideal setup would allow in-situ measurement of the distance between pistons** and as such the volume of the pellet to track the absolute densification**.** Given that cold-pressing of Na_3PS_4 can routinely result in >95% densified pellets we do not think this assumption is unwarranted.

A second assumption relates to the hydrostatic (isotropic) dissipation of the uniaxially applied pressure. This predisposes that the highly deformable thiophosphate can act as its own pressure transmitting medium. We have observed indentations on the polycarbonate mold corresponding to the sides of the pelletized sample in the radial direction (i.e. perpendicular to the applied force). In extreme cases, this lead to fracture of the polycarbonate mold perpendicular to pressing direction. These observations, on the one hand, support our assumption of isotropic pressure dissipation, while, on the other hand, further underlines the need for a pressure-resistant housing for such experiments. We note that a flattening of the sample pellet inside the mold could lead to significant changes in the form factor of the pellet leading to overestimation of the sample conductivity. The magnitude of this uncertainty does not undermine our conclusions and does not affect the activation volume determination which is irrespective of the form factor of the pellet. **An ideal setup would feature a dedicated hydrostatic pressure medium** such as mineral oil.

Finally, another source of uncertainty pertains to the absence of a direct temperature control or measurement in the current setup. For this study, the temperature in the measurement room was controlled to 23 ± 2 °C and the samples were left to equilibrate for at least 30 minutes before measurement. **An ideal setup would allow simultaneous control of pressure and temperature** to minimize uncertainty and allow study of the dependence of E_a on P and V_a on T for a holistic description of the ion-diffusion characteristics.

References

(1) Toby, B. H. R Factors in Rietveld Analysis: How Good Is Good Enough? *Powder Diffr.* **2006**, *21*, 67–70. https://doi.org/10.1154/1.2179804.

(2) Nose, M.; Kato, A.; Sakuda, A.; Hayashi, A.; Tatsumisago, M. Evaluation of Mechanical Properties of Na_2S–P_2S_5 Sulfide Glass Electrolytes. *J. Mater. Chem. A* **2015**, *3*, 22061–22065. https://doi.org/10.1039/C5TA05590C.

(3) Deng, Z.; Wang, Z.; Chu, I.-H.; Luo, J.; Ong, S. P. Elastic Properties of Alkali Superionic Conductor Electrolytes from First Principles Calculations. *J. Electrochem. Soc.* **2016**, *163*, A67–A74. https://doi.org/10.1149/2.0061602jes.

(4) Yu, Z.; Shang, S.-L.; Seo, J.-H.; Wang, D.; Luo, X.; Huang, Q.; Chen, S.; Lu, J.; Li, X.; Liu, Z.-K.; et al. Exceptionally High Ionic Conductivity in $Na_3P_{0.62}As_{0.38}S_4$ with Improved Moisture Stability for Solid-State Sodium-Ion Batteries. *Adv. Mater.* **2017**, *29*, 1605561. https://doi.org/10.1002/adma.201605561.

(5) Liu, W.; Sun, H.; Niu, Y. Theoretical Investigation the Mechanical and Thermodynamic Properties of α and β-Phase Solid Electrolytes Na_3PS_4. *J. Electrochem. Soc.* **2019**, *166*, A3011–A3018. https://doi.org/10.1149/2.1081913jes.

(6) Wang, H.; Yu, M.; Wang, Y.; Feng, Z.; Wang, Y.; Lü, X.; Zhu, J.; Ren, Y.; Liang, C. In-Situ Investigation of Pressure Effect on Structural Evolution and Conductivity of Na_3SbS_4 Superionic Conductor. *J. Power Sources* **2018**, *401*, 111–116. https://doi.org/10.1016/j.jpowsour.2018.05.037.

(7) Boulineau, S.; Tarascon, J.-M.; Leriche, J.-B.; Viallet, V. Electrochemical Properties of All-Solid-State Lithium Secondary Batteries Using Li-Argyrodite Li_6PS_5Cl as Solid Electrolyte. *Solid State Ionics* **2013**, *242*, 45–48. https://doi.org/10.1016/j.ssi.2013.04.012.